Experimental study on the influence of CO_2 on the microstructure of deformed olivine aggregates

Huihui Zhang[a, b, c], Ningli Zhao[b, *], Xiaoge Huang[a, *], Greg Hirth[b, *]

[a] Institute of Geology and Geophysics, Chinese Academy of Sciences, Beijing 100029, China;
[b] Department of Earth, Environmental and Planetary Sciences, Brown University, Providence, RI 02906, USA;
[c] University of Chinese Academy of Sciences, Beijing 100049, China

Abstract

We conducted high-temperature and high-pressure deformation experiments on hot-pressed aggregates of olivine + 9 wt% dolomite at 1 GPa and 1100ºC in a Griggs-type apparatus. At run conditions, the dolomite decomposed to produce ~7 vol% CO_2 as a supercritical fluid. Microstructural observations show that CO_2 is distributed at triple junctions and as isolated "bubbles" along grain boundaries in the hot-pressed samples. After deformation, the CO_2 is redistributed to form CO_2-rich bands and CO_2-depleted bands. Compared to experiments with the basaltic melt, CO_2 does not reduce olivine viscosity as much. The CPOs of CO_2-bearing samples are much stronger than the CPO of melt-bearing samples, although [100] and [001] axes girdles are found in both types of samples. Olivine is much more soluble in basaltic melt than CO_2, which enhances diffusion accommodated deformation mechanisms more in melt-bearing samples. Our mechanical and microstructural data support the hypothesis that the kinetic effect of a fluid or melt phase depends on the chemistry and fluid topology.

Keyword: olivine, CO_2, rheology, crystallographic preferred orientation

1. Introduction

The rheological properties of peridotite are critical for modeling of the strain localization at plate boundaries, fluid and melt transport, and the velocity and attenuation of seismic waves in the upper mantle. The Earth's mantle is considered to be the largest carbon reservoir. Carbon in the upper mantle can be brought to the oceans and the atmosphere via volcanic activity (Sleep & Zahnle, 2001). The subduction process, especially the subduction of ocean plates, recycles carbon into the upper mantle. The main form of carbon in the upper mantle is carbonate (CO_3^{2-}). However, carbon can also exist as CO_2 or carbonated melt (Dasgupta & Hirschmann, 2010). Russell et al. (2013; 2015) analyzed how CO_2 released by depressurization during the eruption of kimberlite accelerates the transport of kimberlite. Similar to basaltic melt (Hirth & Kohlstedt, 1995; Mei et al., 2002; Holtzman et al., 2012), the

presence of CO_2 may reduce the viscosity of peridotite and affect the deformation microstructure.

The impacts of basaltic melt on peridotite rheology have been studied intensively, yet the rheological influence of other types of the fluid phase, for example, carbonate melt or supercritical CO_2, has not been studied. Conductivity experiments carried out on peridotite show that adding carbonate melt significantly increases the electrical conductivity (Huang et al., 2005; Yoshino et al., 2012), indicating that presence of carbonate melt enhances the transport properties. At certain geological conditions, the carbonate melt will decompose into CO_2 in the lithosphere. For example, CO_2 has been shown to be critical to the ascent and eruption of kimberlite (Wilson & Head, 2007).

The weakening effect of CO_2 on creep behavior depends on its distribution and geometry. Hydrostatic studies show that the CO_2/olivine dihedral angles are generally in excess of 60º (up to 90º; Watson & Brenan, 1987), which is significantly greater than that of the basalt/olivine (30º-50º; Bulau et al., 1979; Waff & Bulau, 1979; Cooper & Kohlstedt, 1982). Therefore, the supercritical CO_2 would form isolated CO_2 pocket along grain boundaries at low volume fractions (von Bargen & Waff, 1986; Mibe, 1998). The tendency of CO_2 forming isolated pockets indicates that the weakening effect of CO_2 may not be as significant as that of basaltic melt. In addition, the lower solubility of olivine in CO_2 would limit the degree of creep enhancement resulting from enhanced (short-circuit) diffusion in the fluid phase (Cooper & Kohlstedt, 1986).

We used a Griggs-type deformation apparatus to shear CO_2-bearing peridotite. To produce CO_2, we mixed dolomite into olivine and pyroxene aggregates. Under the experimental conditions, dolomite decomposed into CO_2; excess CaO and MgO will react with low-Ca pyroxene and olivine to form high-Ca pyroxene and monticellite. Ignoring FeO, the simplified reaction will be (Canil & Scarfe, 1990):

$$3\ CaMg(CO_3)_2 + 2\ Mg_2Si_2O_6 = 2\ CaMgSiO_4 + MgCaSi_2O_6 + 4\ MgO + 2\ CO_2.$$

$$CaMg(CO_3)_2 + Mg_2SiO_4 = CaMgSiO_4 + 2\ MgO + 2\ CO_2$$

2. Experimental methods

2.1 Sample preparation and deformation experiments

Olivine (Ol) and clinopyroxene (CPx, with ~8 wt% of orthopyroxene; Zhao et al., 2019) grains were hand-picked from a lherzolite xenolith (Damaping, Hebei, China). Ol and CPx grains were separately ground in an agate motor and sieved to obtain a grain size of 20-32 μm. The Ol and CPx powders were subsequently baked in a controlled atmosphere furnace at 850ºC for 20 hours at an oxygen fugacity set by flowing one-to-one ratio of CO and CO_2, which is within the stability field of Fo_{90} (f_{O_2} = 10^{-14} Pa). Ol powder was mechanically mixed with 3 wt% CPx and 9 wt% dolomite with a grain size of 20-32 μm that can supply 7 vol% CO_2. We estimated the CO_2 volume fraction for each annealed sample by assuming that all the pore spaces observed in micrographs were occupied by CO_2. This assumption may overestimate the CO_2 volume fraction, because of porosity produced during polishing. Calculated

CO_2 fraction based on mass balance of dolomite and peridotite reaction are generally consistent with the estimate based on microstructure. The estimation of the CO_2 fractions is given in Supplementary Table 1.

Specimens were prepared by cold-pressing 0.1 g of the powder mixture into a nickel can between two alumina pistons beveled at 45º. The details of the experimental assembly are described in Zhao et al. (2019). The cold-pressed samples were stored in a vacuum oven at 110ºC for more than 6 hours before experiments. Cold-pressed samples were then hot-pressed at 1100ºC and a confining pressure of 1 GPa for 16-18 hours in a Griggs-type apparatus, and then deformed at the same pressure and temperature. We performed four types of experiments: hot-press experiments, constant displacement rate experiments, displacement rate stepping experiments, and post-deformation annealing experiments. For the three types of experiments involving deformation, samples were all initially deformed at the displacement rate of 7.5×10^{-5} mm/s. Two samples (W2264, W2266) were deformed to a shear strain of $\gamma \approx 3$ in constant displacement experiments. W2266 was deformed to $\gamma \approx 3$ and then annealed *in situ* for 10 hours at 1100ºC and 1 GPa. A strain rate stepping experiment (W2263) was carried out at displacement rates of 6.0×10^{-5} mm/s, 1.6×10^{-5} mm/s, 1.9×10^{-4} mm/s, and 7.9×10^{-5} mm/s to total shear strains of $\gamma = 5$. We also deformed two dolomite-free dunite samples. At the end of the experiment, the samples were quenched to 300ºC in 12 min. Then, the confining pressure was decreased while removing the load simultaneously. During depressurization, a differential stress of about 100 MPa was maintained on the sample to minimize unloading cracks. The temperature was then lowered to the temperature of the cooling water (19ºC).

Once the sample was removed from the apparatus, we observed that many "blisters" started to appear on the surface of the Ni jackets. When the sample was submerged into ethanol, and Ni jacket was pierced, we observed gas bubbles released from the blisters for several minutes – indicating the assemblies successfully encapsuled CO_2 gas within the jacket at our experimental conditions. Infrared absorption spectrometry (FTIR) results on a hot-pressed 7 wt% CO_2 sample show that the olivine aggregate (including grain boundaries) contained ~9 ppm H_2O by weight (~150 H/10^6 Si), and indicate samples are almost "dry" prepared through this procedure. FTIR results are presented in Supplementary Figure 1.

We calculated the shear strain rate using the applied displacement rate divided by the measured thickness of samples. Comparison of hot-pressed and deformed specimens indicates that sample thickness decreases from ~1.3 mm to ~0.9 mm after a shear strain of $\gamma = 4$, which increases shear strain rate by 40% (Supplementary Figure 2). von Mises equivalent strain rate (refer to as equivalent strain rate for the remainder of the paper) was obtained by dividing shear strain rate by $\sqrt{3}$. Shear stresses were corrected by subtracting the contribution from friction within the assembly (e.g., Zhao et al., 2019). von Mises equivalent stresses (refer to as equivalent stress for the remainder of the paper) were obtained by multiplying shear stresses by a factor of 2.

2.2 Microstructural analysis

Microstructures were studied using optical microscopy, scanning electron microscopy (SEM), and electron backscatter diffraction (EBSD). Most of the samples were cut parallel to the shear direction and perpendicular to the shear plane (referred to as "XZ plane"). Two deformed samples were cut parallel to the shear plane. The nickel jacket and alumina pistons were removed before polishing. We dry-polished the sample wafer on 30 μm, 15 μm, 6 μm, 3 μm, 1 μm, and 0.5 μm diamond lapping film. To protect deformation microstructures of the highly porous samples, water, ethanol or any fluids were avoided during mechanical polishing. Thin sections prepared for EBSD were subsequently polished in colloidal silica. Some of the thin sections were etched in phosphoric acid for 45 minutes to highlight grain boundaries. We quantified grain sizes based on the EBSD map and approximated the grain size by multiplying the mean intercept length by a factor of 1.5 (Gifkins, 1970). For comparison, we also calculated the grain size using equivalent circular diameters multiplied by a factor of $4/\pi$ (Heilbronner & Barrett, 2014). Grain sizes obtained by these two methods are shown in Supplementary Table 2 and Table 3. Grain sizes calculated using these two methods resulted in very similar results except for a hot-pressed sample and an annealed sample.

EBSD analyses were performed by using a Zeiss Sigma field emission scanning electron microscope equipped with an Oxford Instruments Nordlys Nano EBSD detector in the State Key Laboratory of Earthquake Dynamics at Institute of geology China Earthquake Administration. Only W2264 is analyzed using a Tescan MIRA3 LMU field emission scanning electron microscope equipped with an Oxford Instruments NordlysMax2 EBSD detector in the Department of Earth and Environmental Sciences Boston College. The electron beam was rastered across a carbon-coated (4-nm-thick carbon coating) thin section with an accelerating voltage of 15 kV and a step size of 0.5 μm. The resultant EBSD data were analyzed using version 5.3.1. of the MTEX (Bachmann et al., 2010) toolbox for textural analysis in MATLAB. The methods of grain reconstructions and CPO analyses were described in detail by Zhao et al. (2019).

3. Results

3.1 Mechanical data analysis

Mechanical data of general shear experiments are summarized in Supplementary Table 2. The mechanical behavior is analyzed assuming a power law equation with the form:

$$\dot{\varepsilon} = A\sigma^n d^{-p} \exp(\alpha\varphi)\exp(-H/RT), \quad (1)$$

where $\dot{\varepsilon}$ is strain rate, A is a constant, σ is differential stress, n is the stress exponent, d is grain size, p is the grain size exponent, α is a constant, φ is fluid

fraction, H is the activation enthalpy, R is the gas constant, and T is the temperature in Kelvin.

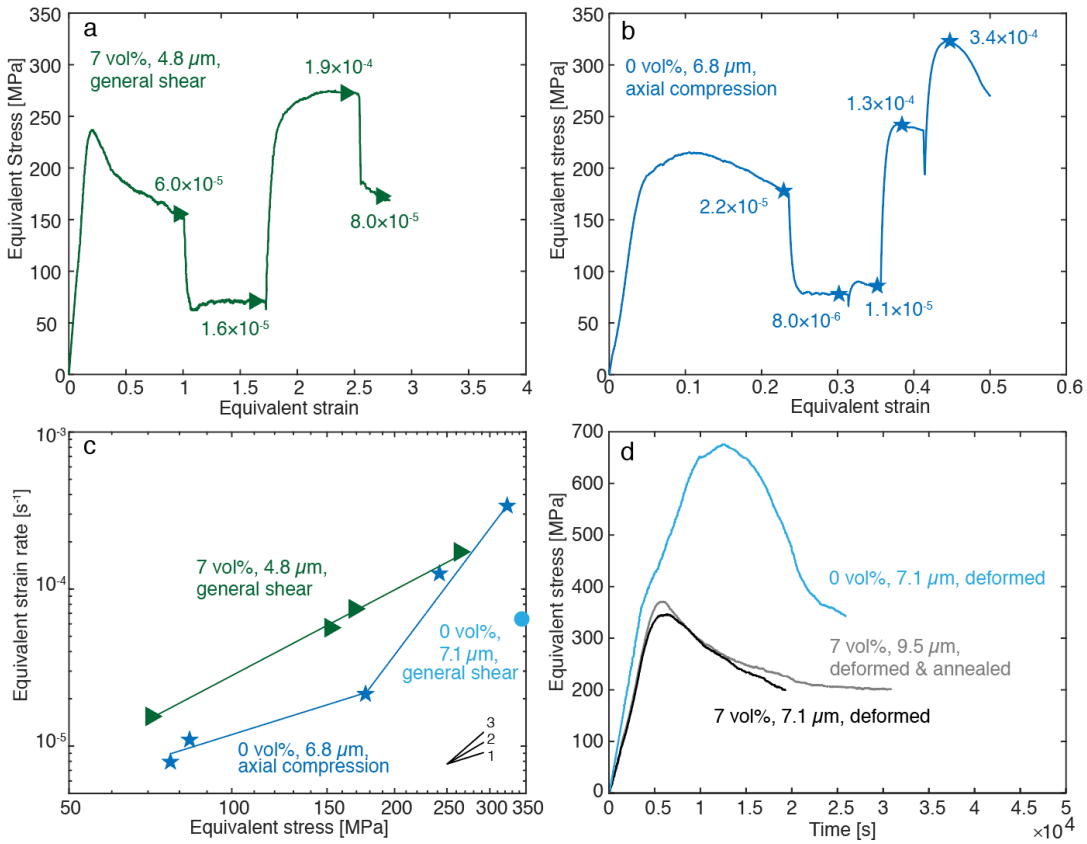

Figure 1. Mechanical data for deformation experiments with 7 vol% CO_2 and CO_2-free dunite with final grain size and experiment type noted in each panel. (a) Equivalent stress versus equivalent strain plot for rate-stepping experiment with 7 vol% CO_2 (W2263) deformed in general shear. Strain rates (s^{-1}) are noted for each step. (b) Equivalent stress versus equivalent strain plot for rate-stepping experiment on CO_2-free dunite sample (W2430) deformed in axial compression. The green triangles in (a) and blue stars in (b) are illustrated where nominally steady-state stress and strain rate values are determined; the data of these two experiments as well as an experiment on CO_2-free experiment are plotted in (c). (d) Equivalent stress versus time plots for general shear experiments conducted at a strain rate of about 8.0×10^{-5} s^{-1}. The blue line represents a 0 vol% CO_2 experiment (W2271). The black and grey lines represent two 7 vol% CO_2 experiments (W2264 and W2266, respectively). The sample (W2266) are annealed for 10 hours at 1 GPa and 1100ºC.

The equivalent stress versus equivalent strain curves for CO_2-bearing and CO_2-free olivine aggregates are presented in Figures 1a and 1b, respectively. The flow stress for the 7 vol% CO_2 sample is lower than that for CO_2-free dunite samples at the same strain rate, but the difference is within a factor of two. A linear fit to the data in Figure 1a gives a stress exponents n = 1.8 (R^2 = 0.998) for the CO_2-bearing sample. For the axial compression experiment on the CO_2-free dunite sample, we obtain a stress exponent of 1.0 for the three slower strain-rate steps and 4.6 for the faster strain-rate steps, indicating a transition in deformation mechanism at a stress of ~200 MPa (Figure 1c). All the experiments show significant strain weakening. The

magnitude of strain weakening is highest in the general shear experiment on CO_2-free dunite sample (Figure 1d); the weakening slope is also greatest in the CO_2-free sample (all experiments in Figure 1d were carried out at the same strain rate).

3.2 Microstructure

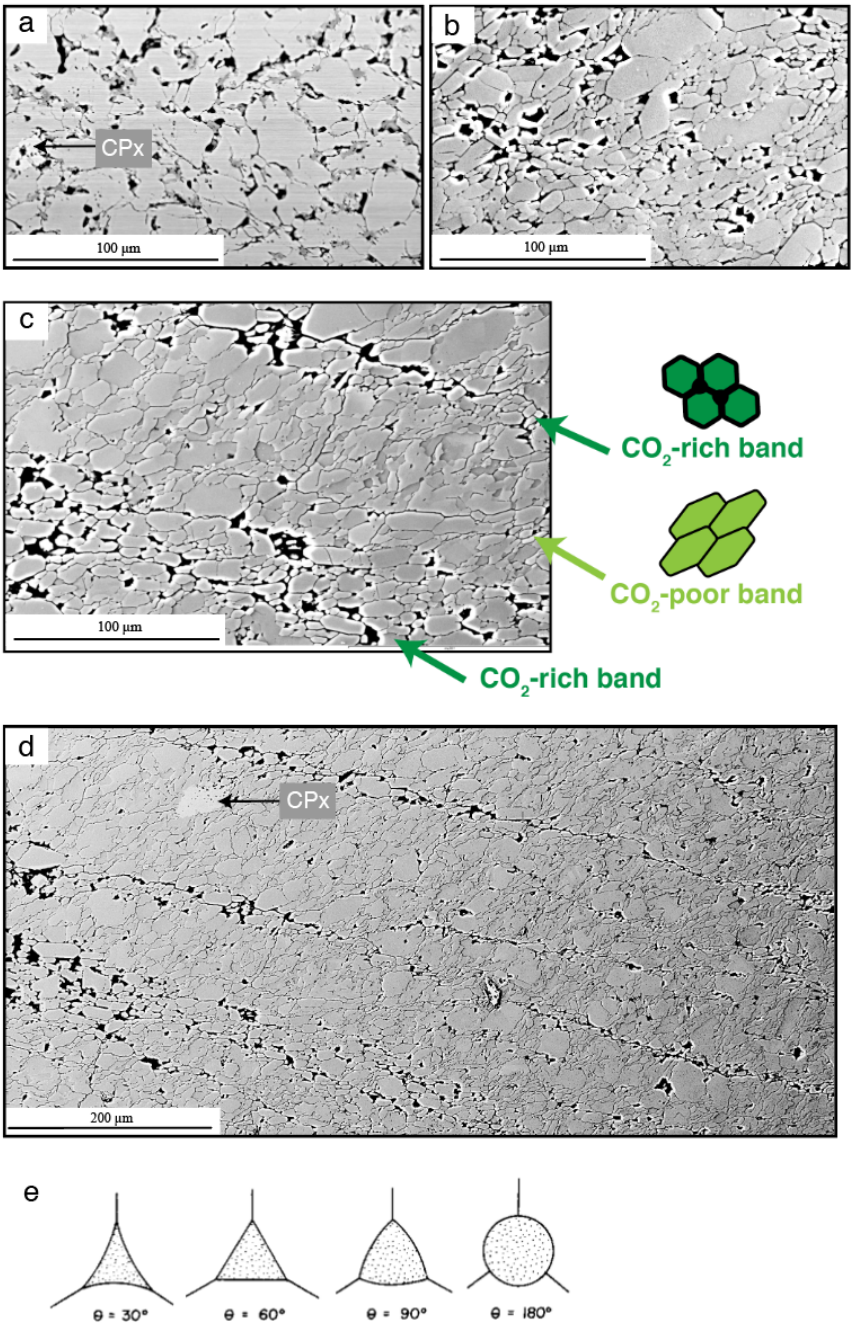

Figure 2. Backscattered electron (BSE) images of 7 vol% CO_2 samples. (a) Hot-pressed sample, W2261. (b) Deformed & annealed sample, W2266. (c) Deformed sample, W2264. (d) A low-magnification micrograph of W2264. The majority of the grey phase in the BSE is olivine, with a minor amount of contrast caused by orientation. The darkest spots on the grain boundaries are pores (formerly CO_2-filled). A few CPx grains (light grey) are observed in (a) and (d). (e) Channel

cross-sections for several values of wetting angles (30º, 60º, 90º, and 180º) from Watson & Brenan (1987).

Micrographs of etched thin sections show the distribution of porosity; we assume that these pores were filled with CO_2 during the experiments. In the hot-pressed and the "deformed & annealed" samples (Figure 2a and 2b), the size of some of the large CO_2 pockets are close to the lower limit of the olivine grain size. Apparently, smaller (maybe due to the thin-section effect) CO_2 pockets are sparsely and homogenously distributed at olivine triple junctions, and as isolated "bubbles" along the olivine grain boundaries. The shape of the CO_2 pockets in Figure 2 indicates that the wetting angles between olivine and CO_2 greater than for olivine and basaltic melt. The presence of CO_2 pocket at triple junctions arises because of a relatively high fraction of CO_2 (> 5 vol%), which is consistent with observations of von Bargen & Waff (1986). Both the shape and distribution of CO_2 pockets are consistent expectations based on wetting characteristics.

The distribution of CO_2 changes dramatically in deformed samples (Figures 2c and 2d). At lower magnification, CO_2 rich bands are observed that extend across almost the entire section. The fluid segregation forms ~30-µm-wide CO_2-rich bands and ~100-µm-thick CO_2-depleted bands oriented ~20º from the shear plane (forming C' bands), on the opposite side of the shear plane from the long axis of the finite strain ellipsoid (FSE). The porosity in the CO_2-depleted bands is similar to that observed in the dolomite-free dunite samples (Supplementary Figure 3). Similar redistribution of a fluid or melt phase during shear deformation of peridotite has been observed in several other studies (e.g., Holtzman et al., 2012; Qi et al., 2018).

Grain sizes in deformed samples are smaller than hot-pressed samples or "deformed & annealed" samples (Supplementary Table 2). In the CO_2-rich bands, olivine grains are elongate parallel to the band, and tend to be aligned subparallel to the shear plane; in the CO_2-depleted bands, olivine grains are elongated in the "S-foliation," sub-perpendicular to the CO_2-rich bands.

3.3 Crystallographic preferred orientations

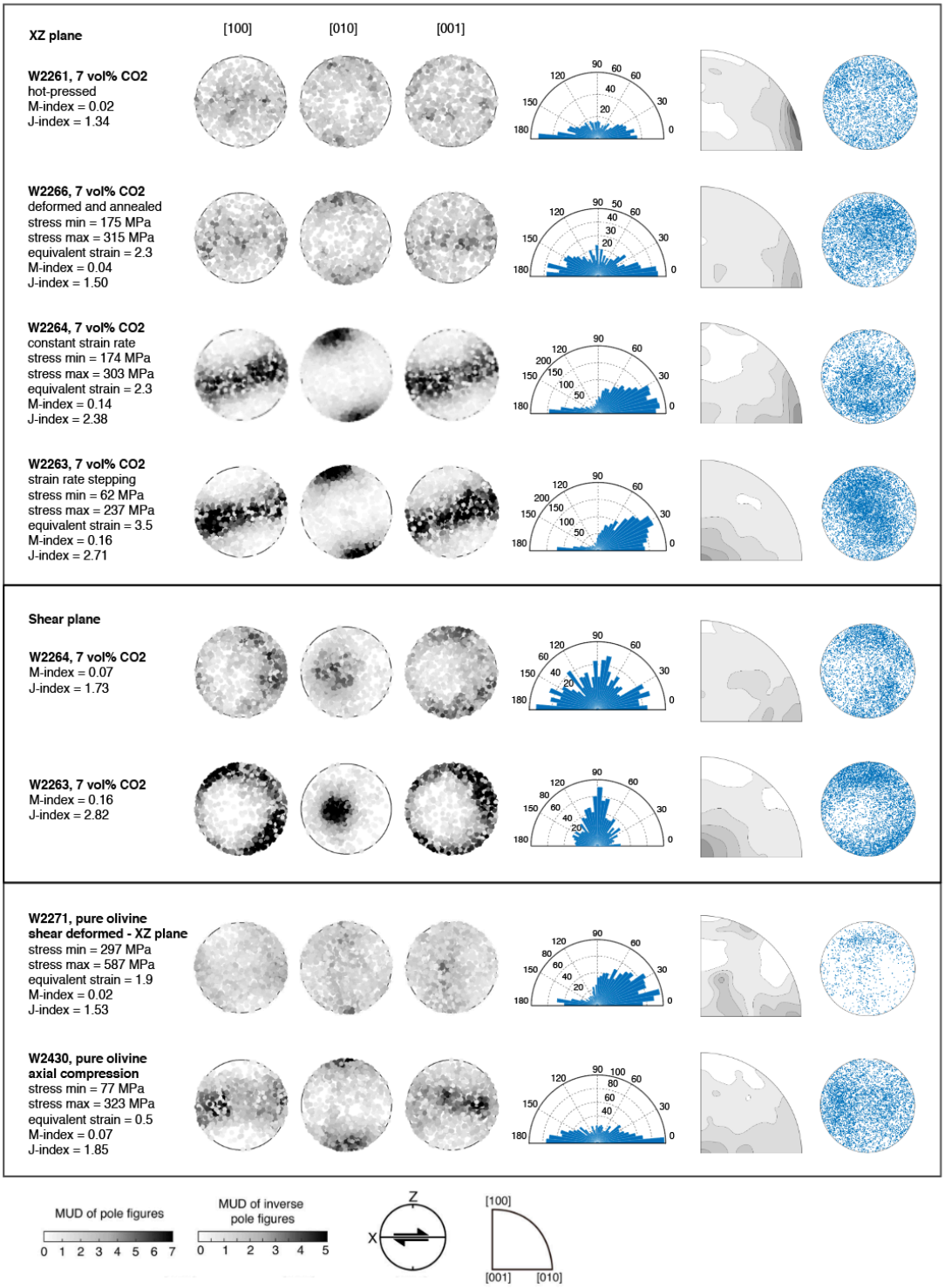

Figure 3. Pole figures of crystallographic orientations, histograms of shape preferred orientation, inverse pole figures of intragranular misorientation axis distribution in the crystal reference frame, and intragranular misorientation axis distribution in the sample reference frame. Pole figures are equal area, upper-hemisphere projection of olivine crystal axes. CPO of olivine grains is measured for 1 hot-pressed sample (W2261), 4 sheared samples (W2263, W2264, W2266, and W2271), and 1 compressed sample (W2430) with EBSD analysis. Grey scale or color scale indicates the multiples of a uniform distribution (MUD). Samples are sheared top to the right.

The hot-pressed 7 vol% CO_2 sample has a very weak CPO, with [010] axes sub-perpendicular to the shear plane. Strong olivine axial-girdle (AG-type) fabrics are observed in the deformed 7 vol% CO_2 samples. The [100] and [001] axes are distributed in a plane oriented approximately 20º antithetic to the shear plane; [010] axes are subnormal to the shear plane. The symmetry of the fabric is similar in the deformed & annealed sample, but the M-index decreases significantly from ~0.15 to 0.04 in the annealed sample. The CPO of the sheared CO_2-free dunite sample shows olivine [100] axes parallel to the shear plane in the shear direction, and [010] axes are subnormal to the shear plane. The fabric strength is surprisingly weak, given that the sample was deformed to the same strain at higher stress. The CO_2-free dunite sample deformed in axial compression has a slightly stronger CPO with [010] axes aligned parallel to the compression direction.

Intragranular misorientation axes of samples deformed to an equivalent strain of lower than 3 clusters around [010]; the sample deformed to an equivalent strain of 3.5 shows a cluster around [001]. The strain-dependent transition of misorientation axes is consistent with observations in CO_2-free dunite deformed to various strains (Hansen et al., 2014). Misorientation axes in the sample reference frame show that most of the misorientation axes are within the shear plane and perpendicular to the shear direction, suggesting that these misorientation axes are rotations axes for tilt boundaries. Therefore, the [010] misorientation axes indicate the climb of (001)[100] dislocations, and [001] misorientation axes indicate the climb of (010)[100] dislocations.

The XZ plane section shows that the overall CPO of the deformed samples with CO_2 is an AG-type or an axial [010]-type texture (e.g., Chatzaras et al., 2016; Figures 4a, 4b, and 4c). Closer inspection shows that the girdles comprised different components that correlate with the 2D aspect ratio of the grains in the XZ plane section. High aspect ratio grains exhibit strong A-type fabric, while low aspect ratio grains exhibit strong B-type fabric. For A-type fabric, the [100] maximum is oriented sub-parallel to the shear direction (back rotated 20º), the [010] maximum is oriented sub-perpendicular to the shear plane (again back rotated 20º), and the [001] maximum is oriented within the shear plane and perpendicular to the shear direction. The B-type fabric component has the same geometry, with the [100] and [001] exchanged. Although the CPOs are different, the intragranular misorientation axes of three groups of grains all clustered around [010] axes, with a minor concentration at [001]. Misorientation axes parallel to [010] are consistent with tilt boundaries from (001)[100] slip, and misorientation axes parallel to the [001] axes are consistent with tilt boundaries from (010)[100] slip.

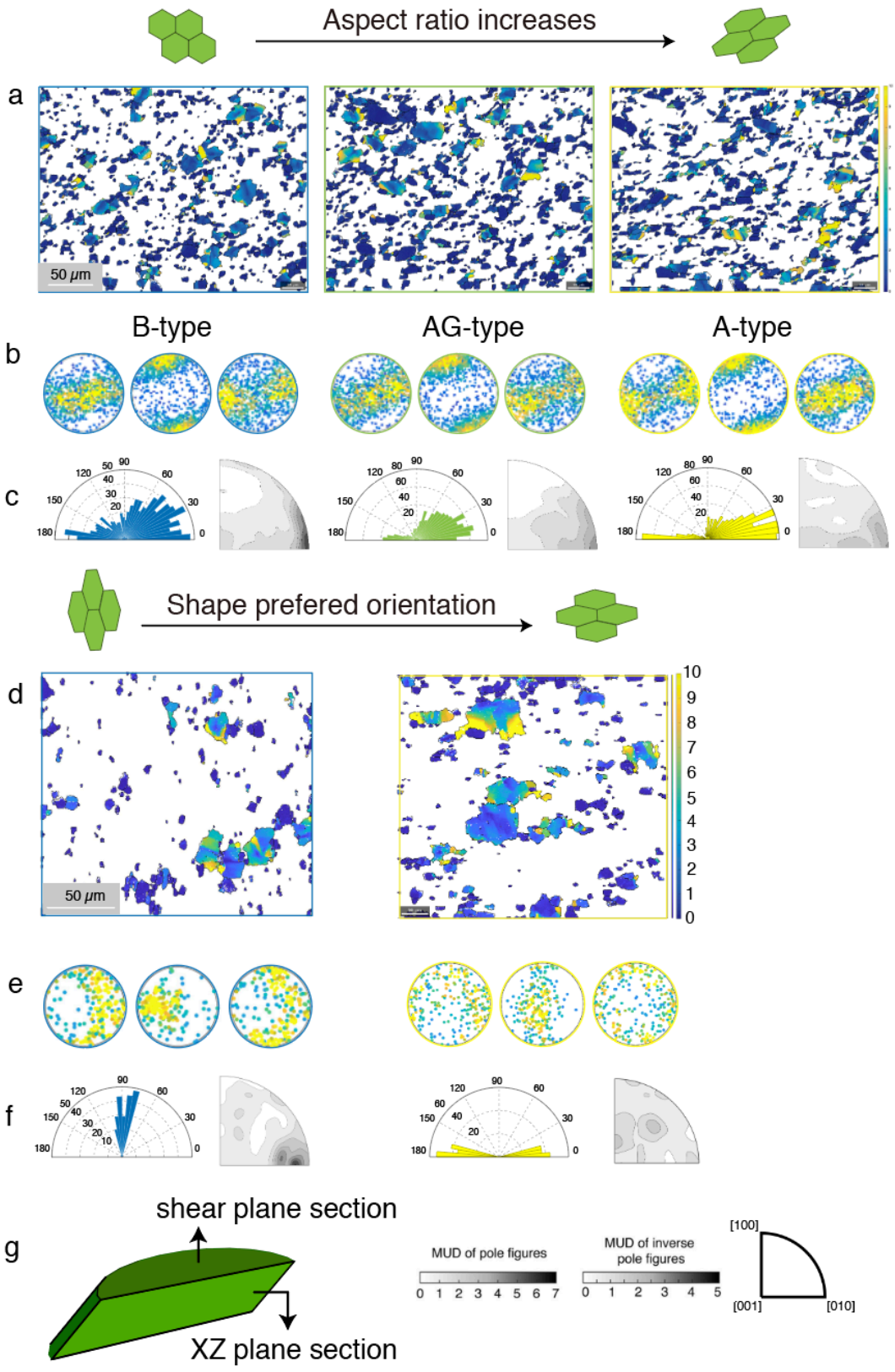

Figure 4. EBSD maps and microstructural analyses of 7 vol% CO_2 deformed sample (W2264; The 7 vol% CO2 stepping strain sample (W2263) show in Supplementary Figure 4). a, b, and c, the XZ plane section. d, e, and f, the shear plane section. g, the schematic figure of the XZ plane and

shear plane section. Grains in the map are sorted according to either aspect ratios (XZ plane section; from left to right, the aspect ratio of grains increases.) or shape preferred orientations (shear plane section; long axes of grains are either parallel to the shear direction or perpendicular to the shear direction). The color of each pixel inside grain maps represents the misorientation between each pixel and the mean orientation of the grain that the pixel belongs to. Pole figures are equal area, upper-hemisphere projection of olivine crystal axes, and the color scale indicates the multiples of a uniform distribution (MUD).

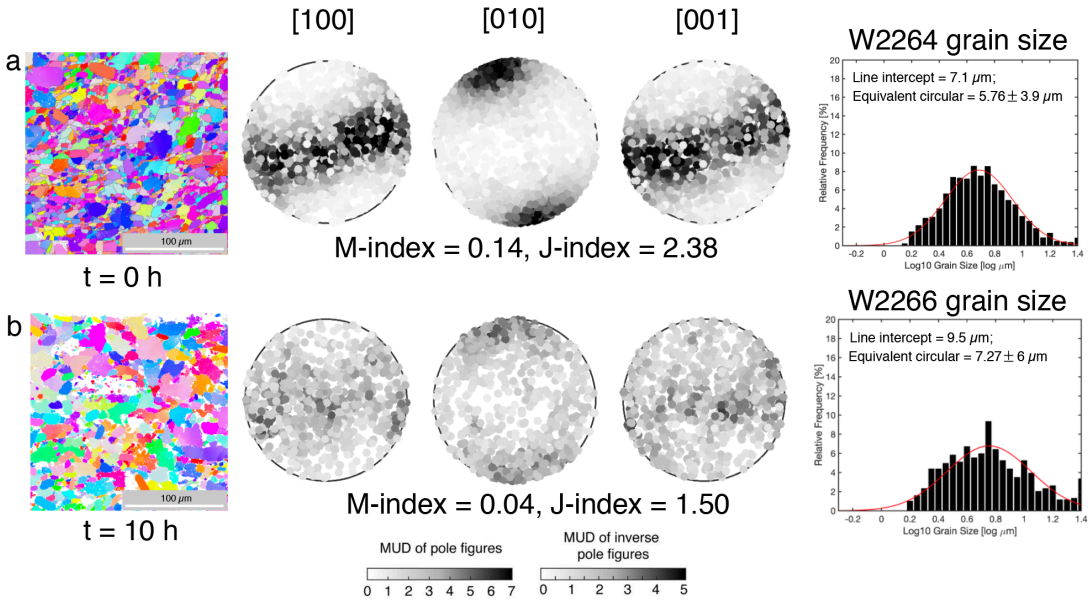

Figure 5. EBSD maps and grain size histograms of a deformed (W2264) and a "deformed & annealed" sample (W2266) with 7 vol% CO_2.

Grains in the shear plane section are sorted according to the 2D shape preferred orientation (i.e., the orientation of the long axes; Figures 4d, 4e, and 4f). As shown in the rose diagram, the long axes of the group of grains on the lower left panel of Figure 4f are perpendicular to the shear direction (75-105º); the olivine [010] of these grains are between the shear direction and the pole of the shear plane. Accordingly, the [100] and [001] axes girdles are subparallel to the shear plane, which is back-rotated from the finite strain ellipse. These observations indicate that the "B-type" grains in Figure 4a do not represent grains that are elongated perpendicular to the shear direction by [001] or [100] slip. In contrast, the [010] axes of the other group of grains (with long shape axes parallel to the shear direction) are parallel to the pole of the shear plane; their [100] and [001] axes are distributed in a plane parallel to the shear plane.

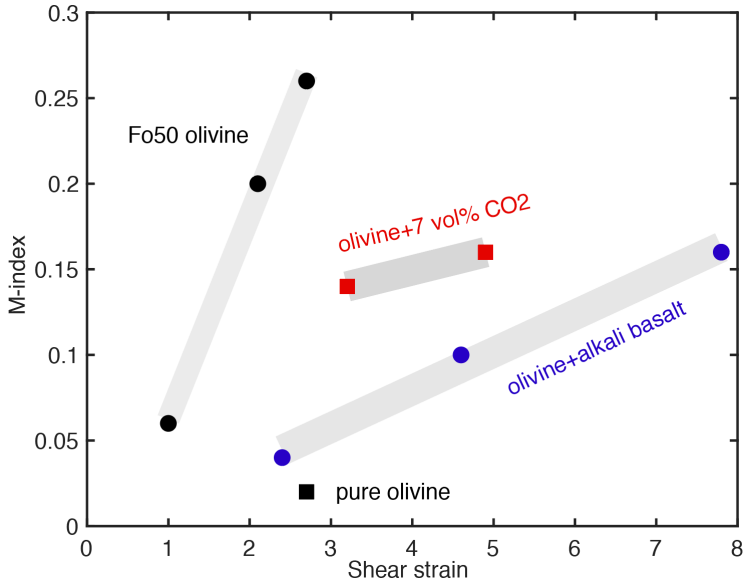

Figure 6. M-index as a function of shear strain. Red squares represent the 7 vol% CO_2 samples (W2263; W2264), and the black square represents the CO_2-free olivine sample (W2271) from this study. Blue dots represent the melt-bearing olivine samples from Qi et al. (2018). Black dots represent the aggregates of Fo_{50} olivine from Hansen et al. (2014).

Figure 5 shows the effect of post-deformation annealing on microstructures. The sample annealed after deformation for 10 hours at 1 GPa and 1100ºC has a significantly weaker CPO. The M-index for the annealed sample is 0.04, while the M-index of the sample quenched after deformation to the same strain without annealing is 0.14. This observation indicates that the rate of weakening of CPO is much faster than reported by Boneh et al. (2017) for annealing melt-free dunite samples. The grain size increased modestly from 7 μm to 10 μm, and the grain size distribution is more bimodal in the annealed sample.

The CPO strength of the one CO_2-free shear sample in our study is lower than that observed in general shear or torsion experiments in other studies on either melt-free or melt-bearing aggregates (Figure 6). The low CPO strength could be caused by a significant contribution from diffusion creep in this sample. The activity of diffusion creep is also suggested by a lower average grain aspect ratio (1.49) than observed for the two 7 vol% CO_2 sample (1.64 and 1.60). In contrast, at the same deformation conditions, the CPO strength of 7 vol% CO_2 samples is stronger than olivine + basalt dunite samples (Qi et al., 2018) deformed to the same strain, and is close to the CPO strength of CO_2-free dunite samples in Hansen et al. (2014). Basaltic melt effectively enhances intergranular deformation (grain boundary sliding, GBS) by increasing the grain boundary stress (Hirth & Kohlstedt, 2003), which causes a stronger than predicted rheological weakening, and the activation of grain boundary sliding may correspondingly produce a weaker CPO. However, the wetting angle of CO_2 is much higher and is expected to promote a weaker weakening effect for CPO development (i.e., stronger CPO strength). This scenario is consistent with the observations that

CO_2-bearing samples showed only modestly lower viscosities than the CO_2-bearing dunite samples.

4. Discussion

4.1 Comparison of the effect of CO_2 and basaltic melt on the microstructure development

After deformation, isolated CO_2 pockets become interconnected and formed the CO_2-rich bands subparallel to the shear plane, oriented at an angle approximately 20º synthetic to the shear plane. The alignment of the CO_2-rich bands is similar to those observed in deformed basalt-melt-bearing or gold-bearing olivine aggregates (Bruhn et al., 2000; Holtzman et al., 2003). This observation supports the hypothesis that stress-driven melt (or other weak secondary phases) segregation is controlled by deformation geometry and stress rather than chemical composition or interfacial energy (Bruhn et al., 2000).

As extremely weak secondary phases, CO_2 and basaltic melt influence CPO development of dunite in similar ways. However, the strength of CPOs in the CO_2-bearing dunite samples are stronger than in the basaltic-melt-bearing dunite samples (Figure 6), possibly because of the intrinsic difference in the kinetic effect of CO_2 and basaltic melt. Dislocation glide is usually expected to control CPO development (Karato et al., 2008). However, the addition of basaltic melt likely increases the fraction of strain accommodated by diffusion accommodated creep and GBS, thus reducing the activation of dislocation glide mechanism (Holtzman et al., 2003). However, components of olivine are less soluble in CO_2 or carbonate melt (Kamenetsky & Yaxley, 2015) compared to basaltic melt. Thus, the enhancement of diffusion accommodated creep may not be as prominent. Therefore, the CPO strength of CO_2 added samples is greater than that of basaltic melt added samples (Figure 6).

Similar to melt-bearing samples, we observed 20º back-rotation of [100] axes from the shear direction in CO_2-bearing samples, likely caused by CO_2 segregation (Figures 2c and 2d) and strain partitioning in the CO_2-bearing band (Holtzman et al., 2003).

Figure 3 and Figure 4 indicate that there is a significant component of B-type fabric in the CPO of 7 vol% CO_2 samples, similar to Holtzman et al. (2003) and Qi et al. (2018). Macroscopically, samples are 30% thinner when shear strain reaches 4 (Supplementary Figure 2). Shear strain is partitioned into CO_2-rich bands, thus the intracrystalline creep of CO_2-poor regions accommodate a greater component of triaxial shortening. If the sample wafer is circular, then shortening would cause the sample to elongate in the shear direction and the norm of shear direction within the shear plane (note as Y direction) by the same amount. However, because of the geometry of the shear piston and shear strain, the sample is longer in the shear direction than in the Y direction. Therefore, during compression, the pressure gradient is greater in the Y direction, and the sample preferentially elongates in the Y direction. This component of strain will cause olivine grains elongated on the Y direction and cause [100] axes to be parallel to the Y direction (Karato et al., 2008),

consistent with the B-type CPO of low-aspect-ratio grains in Figure 4b. The other component of the compaction strain elongates olivine grains subparallel to the X direction and causes [100] axes to be subparallel to the shear direction, consistent with A-type CPO of high-aspect-ratio grains in the XZ plane section (Figure 4b).

4.2 Conclusions and Implications

The presence of CO_2 produces only a modest decrease in the viscosity of the olivine aggregate. For a given stress, the presence of 7 vol% of CO_2 increased the strain rate relative to a CO_2-free sample by about a factor of two at stresses lower than 200 MPa (Figure 1c). In comparison, 7 vol% of basaltic melt promotes a factor of eight to 23 increase in strain rate (Hirth & Kohlstedt, 2003). We interpret that the modest enhancement of the creep rate in the CO_2-bearing samples is caused by the enhancement of grain boundary sliding resulting from the grain boundary distribution of CO_2 in the CO_2-rich bands. As described above, because of the limited solubility of olivine in supercritical CO_2, diffusion creep is not enhanced as much as observed in samples with basaltic melt. This indicates the relative enhancement of dislocation creep or dislocation-accommodated grain boundary sliding (relative to diffusion creep) will be greater for the CO_2-bearing aggregates. This hypothesis is consistent with a stronger CPO observed for the CO_2-bearing samples compared to basaltic-melt-bearing samples.

Degassing of CO_2 from peridotite is an important part of the global CO_2 cycling. Our results provide constraints on the rheological effect of CO_2 on peridotite and the influence of deformation on CO_2 segregation. This chemo-mechanical feedback between CO_2 degassing and peridotite deformation has implications for understanding the accelerated ascent of the magma and the evolution of the melt from carbonatitic to kimberlitic compositions (Russell, 2013; Brett et al., 2015). Our results may also be used to evaluate the long-term effect of CO_2 sequestration, which frequently utilizes the carbonization of peridotite (e.g., Matter and Kelemen, 2009). AG-type fabric observed in CO_2-bearing samples indicates a reduced shear-wave splitting in the mantle where the rheology is influenced by CO_2.

Acknowledgments
This work is benefited greatly from discussions with Reid Cooper, Terry Tullis, Yuval Boneh, Eric Burdette, Nir Badt, Leif Tokle, and Pamela Speciala at Brown University. We appreciate Seth Krukenburg for providing access to EBSD, and Kevin Robertson for providing access to FTIR. We thank Yongsheng Zhou and Xi Ma for providing help with EBSD at the Institute of geology China Earthquake Administration. This research was supported by NSF grants XXXXXX to Greg Hirth; NSFC grants 41574089 and 41774096.

References:

Bachmann, F., Hielscher, R., & Schaeben, H. (2010). Texture analysis with MTEX- Free and open source software toolbox. *Solid State Phenomena*, *160*(February), 63–68. https://doi.org/10.4028/www.scientific.net/SSP.160.63

von Bargen, N., & Waff, H. S. (1986). Permeabilities, interfacial areas and curvatures of partially molten systems: Results of numerical computations of equilibrium microstructures. *Journal of Geophysical Research*, *91*(B9), 9261. https://doi.org/10.1029/jb091ib09p09261

Berry, A. J., Hermann, J., O'Neill, H. S. C., & Foran, G. J. (2005). Fingerprinting the water site in mantle olivine. *Geology*, *33*(11), 869–872. https://doi.org/10.1130/G21759.1

Boneh, Y., Wallis, D., Hansen, L. N., Krawczynski, M. J., & Skemer, P. (2017). Oriented grain growth and modification of 'frozen anisotropy' in the lithospheric mantle. *Earth and Planetary Science Letters*, *474*(July), 368–374. https://doi.org/10.1016/j.epsl.2017.06.050

Brett, R. C., Russell, J. K., Andrews, G. D. M., & Jones, T. J. (2015). The ascent of kimberlite : Insights from olivine. *Earth and Planetary Science Letters*, *424*, 119–131. https://doi.org/10.1016/j.epsl.2015.05.024

Watson B., E., & Brenan, J. M. (1987). Fluids in the lithosphere, 1. Experimentally-determined wetting characteristics of CO2H2O fluids and their implications for fluid transport, host-rock physical properties, and fluid inclusion formation. *Earth and Planetary Science Letters*, *85*(4), 497–515. https://doi.org/10.1016/0012-821X(87)90144-0

Bruhn, D., Groebner, N., & Kohlstedt, D. L. (2000). An interconnected network of core-forming melts produced by shear deformation. *Nature*, *403*(6772), 883–886. https://doi.org/10.1038/35002558

Bulau, J. R., Waff, H. S., & Tyburczy, J. A. (1979). Mechanical and thermodynamic constraints on fluid distribution in partial melts. *Journal of Geophysical Research*, *84*(B11), 6102. https://doi.org/10.1029/jb084ib11p06102

Chatzaras, V., Kruckenberg, S. C., Cohen, S. M., Medaris, L. G., Withers, A. C., & Bagley, B. (2016). Axial-type olivine crystallographic preferred orientations: The effect of strain geometry on mantle texture. *Journal of Geophysical Research: Solid Earth*, *121*(7), 4895–4922. https://doi.org/10.1002/2015JB012628

Cooper, R. F., & Kohlstedt, D. L. (1982). Interfacial energies in the olivine basalt system. *High-Pressure Research in Geophysics*, (January 1982), 217–228. https://doi.org/10.1007/978-94-009-7867-6_17

Cooper, R. F., & Kohlstedt, D. L. (1986). Rheology and structure of olivine-basalt partial melts. *Journal of Geophysical Research*, *91*(B9), 9315. https://doi.org/10.1029/jb091ib09p09315

Dasgupta, R., & Hirschmann, M. M. (2010). The deep carbon cycle and melting in Earth's interior. *Earth and Planetary Science Letters*, *298*(1–2), 1–13. https://doi.org/10.1016/j.epsl.2010.06.039

Demouchy, S., Ishikawa, A., Tommasi, A., Alard, O., & Keshav, S. (2015). Characterization of hydration in the mantle lithosphere: Peridotite xenoliths from the Ontong Java Plateau as an example. *Lithos*, *212–215*, 189–201. https://doi.org/10.1016/j.lithos.2014.11.005

Ferriss, E., Plank, T., & Walker, D. (2016). Site-specific hydrogen diffusion rates during clinopyroxene dehydration. *Contributions to Mineralogy and Petrology*, *171*(6), 1–24. https://doi.org/10.1007/s00410-016-1262-8

Hansen, L. N., Zhao, Y. H., Zimmerman, M. E., & Kohlstedt, D. L. (2014). Protracted fabric evolution in olivine: Implications for the relationship among strain, crystallographic fabric, and seismic

anisotropy. *Earth and Planetary Science Letters*, *387*, 157–168. https://doi.org/10.1016/j.epsl.2013.11.009

Hirth, G., & Kohlstedt, D. L. (1995). Experimental constraints on the dynamics of the partially molten upper mantle: deformation in the diffusion creep regime. *Journal of Geophysical Research*, *100*(B2), 1981–2001. https://doi.org/10.1029/94JB02128

Hirth, G., & Kohlstedt, D. (2003). Rheology of the Upper Mantle and the Mantle Wedge : A View from the Experimentalists.

Holtzman, B. K., Kohlstedt, D. L., Zimmerman, M. E., Heidelbach, F., Hiraga, T., & Hustoft, J. (2003). Melt segregation and strain partitioning: Implications for seismic anisotropy and mantle flow. *Science*, *301*(5637), 1227–1230. https://doi.org/10.1126/science.1087132

Holtzman, B. K., Groebner, N. J., Zimmerman, M. E., Ginsberg, S. B., & Kohlstedt, D. L. (2003). Stress-driven melt segregation in partially molten rocks. *Geochemistry, Geophysics, Geosystems*, *4*(5), n/a-n/a. https://doi.org/10.1029/2001GC000258

Holtzman, B. K., King, D. S. H., & Kohlstedt, D. L. (2012). Effects of stress-driven melt segregation on the viscosity of rocks. *Earth and Planetary Science Letters*, *359–360*, 184–193. https://doi.org/10.1016/j.epsl.2012.09.030

Huang, X., Xu, Y., & Karato, S. I. (2005). Water content in the transition zone from electrical conductivity of wadsleyite and ringwoodite. *Nature*, *434*(7034), 746–749. https://doi.org/10.1038/nature03426

Kamenetsky, V. S., & Yaxley, G. M. (2015). Carbonate-silicate liquid immiscibility in the mantle propels kimberlite magma ascent. *Geochimica et Cosmochimica Acta*, *158*, 48–56. https://doi.org/10.1016/j.gca.2015.03.004

Karato, S., Jung, H., Katayama, I., & Skemer, P. (2008). Geodynamic Significance of Seismic Anisotropy of the Upper Mantle : New Insights from Laboratory Studies. https://doi.org/10.1146/annurev.earth.36.031207.124120

Mei, S., Bai, W., Hiraga, T., & Kohlstedt, D. L. (2002). Influence of melt on the creep behavior of olivine-basalt aggregates under hydrous conditions, *Earth and Planetary Science Letters, 201*, 491–507.

Mibe, K. (1998). Connectivity of aqueous fluid in the Earth's upper mantle, *25*(8), 1–6.

Qi, C., Hansen, L. N., Wallis, D., Holtzman, B. K., & Kohlstedt, D. L. (2018). Crystallographic Preferred Orientation of Olivine in Sheared Partially Molten Rocks: The Source of the "a-c Switch." *Geochemistry, Geophysics, Geosystems*, *19*(2), 316–336. https://doi.org/10.1002/2017GC007309

Russell, J. K. (2013). Kimberlite : rapid ascent of lithospherically modified carbonatites Kimberlite : Rapid Ascent of Lithospherically, (December 2015). https://doi.org/10.1007/978-81-322-1170-9

Scarfe, M. (1990). Phase Relations in Peridotite + CO2 Systems to 12 GPa : Implications for the Origin of Kimbefiite and Carbonate Stability in the Earth ' s Upper Mantle, *95*.

Sleep, N. H., & Zahnle, K. (2001). Carbon dioxide cycling and implications for climate on ancient Earth. *Journal of Geophysical Research E: Planets*, *106*(E1), 1373–1399. https://doi.org/10.1029/2000JE001247

Waff, H. S., & Bulau, J. R. (1979). Equilibrium fluid distribution in an ultramafic partial melt under hydrostatic stress conditions, *84*(9). Retrieved from 10.1029/JB084iB11p06109

Wilson, L., & Head, J. W. (2007). An integrated model of kimberlite ascent and eruption. *Nature*, *447*(7140), 53–57. https://doi.org/10.1038/nature05692

Yoshino, T., Mcisaac, E., Laumonier, M., & Katsura, T. (2012). Electrical conductivity of partial molten carbonate peridotite. *Physics of the Earth and Planetary Interiors*, *194–195*, 1–9. https://doi.org/10.1016/j.pepi.2012.01.005

Zhao, N., Hirth, G., Cooper, R. F., Kruckenberg, S. C., & Cukjati, J. (2019). Low viscosity of mantle rocks linked to phase boundary sliding. *Earth and Planetary Science Letters*, *517*, 83–94. https://doi.org/10.1016/j.epsl.2019.04.019